Contents lists available at ScienceDirect

Applied Catalysis B: Environmental

Ni-Co alloy catalyst from LaNi$_{1-x}$Co$_x$O$_3$ perovskite supported on zirconia for steam reforming of ethanol

Lin Zhao [a,b], Tong Han [a,b], Hong Wang [c,**], Lihong Zhang [a,b], Yuan Liu [a,b,*]

[a] Tianjin Key Laboratory of Applied Catalysis Science and Technology, School of Chemical Engineering and Technology, Tianjin University, Tianjin 300072, China
[b] Collaborative Innovation Center of Chemical Science and Engineering (Tianjin), Tianjin 300072, China
[c] School of Chemical Engineering, Inner Mongolia University of Technology, Hohhot 010062, Inner Mongolia, China

ARTICLE INFO

ABSTRACT

The critical problem facing catalysts for the steam reforming of ethanol (SRE) is deactivation due to carbon deposition and/or sintering of the active components. To overcome this problem, a new scheme for designing and preparing Ni-Co alloy catalysts for SRE has been developed in this study using a perovskite-type oxide of LaNi$_{1-x}$Co$_x$O$_3$ as the precursor. According to the scheme, a series of zirconia-supported LaNi$_{1-x}$Co$_x$O$_3$ catalysts were prepared by impregnating ZrO$_2$ with a mixed solution composed of ions consisting of nickel, cobalt, lanthanum and citric acid. After reduction, the Ni-Co alloy nanoparticles were highly dispersed on ZrO$_2$ and modified with La$_2$O$_3$. The bimetallic catalyst exhibited very good catalytic performance for SRE, including high activity, high selectivity to hydrogen and very good stability due to the synergistic catalysis of cobalt and nickel. The synergy between cobalt and nickel led to a higher anti-coking ability compared to the corresponding monometal catalysts, and the bimetallic catalyst exhibited very good anti-sintering ability. This preparation scheme could be extended to the preparation of many other supported bimetallic catalysts because many transitional metal ions can act as the ions of a perovskite-type oxide.

© 2016 Elsevier B.V. All rights reserved.

1. Introduction

Over the years, people have depended on traditional energy sources, such as oil, coal and natural gas, for manufacturing and living. In today's society, the depletion of non-renewable fossil fuels and the increasing energy consumption require the development of new energy sources [1,2]. For example, in China, traditional vehicles are being partially replaced by electric or hybrid vehicles. Solar, wind and tidal sources are renewable energies that are unstable and dependent on the seasons. Therefore, hydrogen energy stands out as a novel alternative energy source. Hydrogen is a renewable secondary energy source that is environmentally friendly with high efficiency when combined with fuel cells [3].

Currently, hydrogen is primarily obtained from hydrocarbons or other organic compounds, and hydrogen production from water is expected to be extensively industrialized in the not too distant future [4]. Ethanol has been used to produce hydrogen due to several advantages. First, ethanol has high hydrogen productivity. In this process, hydrogen is not only generated from ethanol but also partially from the steam. Secondly, ethanol is mainly produced from fermentation of biological resources including agricultural waste and potentially some plants, seaweeds, and so on. The energy in those biomasses come from sun light, therefore bioethanol is an environmentally-friendly energy resource. Third, the process can avoid the separation of ethanol from water because bio-ethanol contains water. Finally, the storage and operation of ethanol are safe.

The primary approach for the production of hydrogen from ethanol involves the steam reforming of ethanol (SRE), and searching for suitable catalysts are important in this process. The previously reported catalysts can be classified into three types [5]. The first type consists of oxide catalysts, such as ZnO, MgO, V$_2$O$_5$ and Al$_2$O$_3$ [6,7]. In general, the catalytic performance of metal oxide catalysts is worse than that of supported metal catalysts due to their serious carbon deposition and low selectivity to hydrogen. The second type consists of noble metal catalysts including Ru, Rh, Pd, Pt and Au [8–11]. Although noble metal catalysts can achieve good catalytic activity at low temperatures, these catalysts are expensive and typically sintered at high temperatures. Therefore, the

---

* Corresponding author at: Tianjin Key Laboratory of Applied Catalysis Science and Technology, School of Chemical Engineering and Technology, Tianjin University, Tianjin 300072, China.
** Corresponding author.
E-mail addresses: hongwang396@126.com (H. Wang), yuanliu@tju.edu.cn (Y. Liu).

dispersion of noble metals and the stability of the catalysts need to be improved. In addition, the dosage of the noble metal needs to be reduced. The third type consists of base metal catalysts, such as Cu-, Co- and Ni-based catalysts [12–16]. The base metal catalysts experience carbon deposition (amorphous carbon-like coke and graphitic carbon-like CNTs) and sintering, which leads to deactivation of the catalysts and is a key challenge for SRE catalysts [17].

To address the carbon deposition issue, several technical routes have been reported. Ethylene is the precursor of coke and is formed by ethanol dehydration. The dehydration reaction tends to occur on acidic sites. Therefore, basic oxides, such as MgO, La_2O_3 and K_2O, have been used as doping agents [18]. For example, K was added to $Co/\alpha-Al_2O_3$, which resulted in a catalyst with improved activity and higher stability than that of $Co/\alpha-Al_2O_3$ [19]. Because the deposited carbon can react with oxygen, supports, such as ceria, that can generate oxygen vacancies have been employed to eliminate the deposited carbon. Xu et al. reported that Co/CeO_2 exhibited very good anti-carbon deposition ability [20]. The third promising solution for improving the stability involves the use of a bimetal catalyst [21]. For example, when Fe was doped into Ni-based catalysts, the stability and ability to prevent coking improved due to the promotion effect of iron for nickel dispersion [22]. In addition, sintering is another reason for the deactivation of the catalysts. Therefore, any method that can increase the dispersion of the active metal nanoparticles is beneficial for improving the stability of the catalysts [23–25].

Among the bimetallic catalysts for SRE, Ni-Co has been the focus of much research [26]. Damyanova et al. reported that Co promoted Ni/Al_2O_3 catalysts exhibited better stability and higher hydrogen yield compared to that of the Ni/Al_2O_3 catalyst [27]. Resini et al. demonstrated that the formation of CH_4 in the SRE was lower on Co–Ni supported on YSZ than that on the corresponding monometallic nickel catalyst. In addition, the formation of Ni-Co could increase the hydrogen yield [28]. Homs et al. reported that the addition of Ni to Co/ZnO had a positive effect on the production of H_2 at low temperatures (<300 °C) and the catalyst stability [29]. In our previous study [30], a perovskite-type oxide (PTO) consisting of a $LaFeO_3$ supported Ni-Co bimetallic catalyst was prepared using a citric acid complexation-impregnation method. This catalyst, which was used for the SRE, exhibited both high selectivity to hydrogen and good stability. The characterization results indicated that Ni-Co was present as a solid solution alloy. In comparison to the corresponding monometal catalysts, the bimetal catalyst exhibited better anti-sintering ability and better anti-carbon deposition ability. The Ni-Co/$LaFeO_3$ catalyst was prepared by reducing $LaFe_{1-x-y}Co_xNi_yO_3$, and the cobalt and nickel ions were uniformly mixed, favoring the Co-Ni alloy formation. Similarly, Co-Ni/La_2O_3 can be prepared by reducing $LaCo_xNi_yO_3$ [31].

However, when using La_2O_3 or $LaFeO_3$ as the support [30–32], the content of catalyst support is limited because both the active components and the support came from the same PTO precursor (i.e., $LaFe_{1-x-y}Co_xNi_yO_3$ or $LaCo_xNi_yO_3$). The limited content of the support resulted in the support having a small surface area. Therefore, the sintering of the Ni-Co active species is inevitable. An effective approach for improving the dispersion of a catalyst is to load the active components on a support that has a high specific surface area. ZrO_2 is a potential support for the SRE due to its high surface area, good thermal stability and oxygen storage capacity [33,34]. In addition, zirconia can be employed as a support for $LaCoO_3$, $LaFeO_3$ and $LaMnO_3$ using the impregnation method [35–37]. To prepare ZrO_2 supported bimetallic Ni-Co, co-precipitation and ordinary impregnation have been employed [27,38]. However, zirconia loading with perovskite-type oxides as the precursor of the bimetallic Ni-Co has not been previously reported.

In this study, $LaNi_{1-x}Co_xO_3$ was loaded on ZrO_2 and used as the catalyst precursor for the SRE based on the following considerations. (1) A crystal of $LaNi_{1-x}Co_xO_3$ is a much large molecule where the elements (i.e., nickel and cobalt) are uniformly dispersed at the atomic level. As a result, after the reduction, nickel and cobalt tend to interact or form an alloy. (2) Similarly, as another result, La_2O_3 was highly dispersed and can act as a promoter for the SRE, which can restrain the sintering and carbon deposition of the catalyst. (3) ZrO_2 is a promising support for bimetallic Ni-Co and possesses a high specific surface area. The design scheme for the catalyst is shown in Fig. 1. For $LaNi_{0.7}Co_{0.3}O_3/ZrO_2$, Ni-Co would be separated from the lattice of $LaNi_{0.7}Co_{0.3}O_3$ in the reduction process to form Ni-Co alloy nanoparticles, which should be well dispersed in the La_2O_3 matrix that is loaded on ZrO_2.

2. Experimental

2.1. Catalyst preparation

The unsupported $LaNi_{0.7}Co_{0.3}O_3$ was prepared by one step citrate complexing method, for details see Ref. [30]. Briefly, nickel, cobalt and lanthanum nitrate with La: (Ni + Co) molar ratio of 1:1 and Ni:Co molar ratio of 7:3 were dissolved in deionized water. Then citric acid with 120% of the total molars of the cations and polyethylene glycol 400 with 20% molar amount of the citric acid was added into the solution. The solution was stirred for 5 h and then concentrated by raising the temperature up to 80 °C at atmospheric pressure until the formation of a spongy solid. The resultant spongy solid was dried at 120 °C for 24 h. The precursor was calcined at 700 °C for 5 h with the temperature increasing rate of 2 °C min^{-1}. The so prepared sample was referred to as L- N-C.
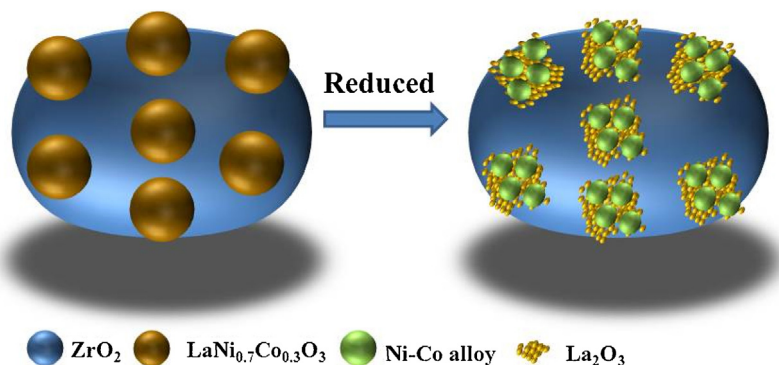

Fig. 1. Schematic representation of the structural evolution of the $LaNi_{0.7}Co_{0.3}O_3/ZrO_2$ catalyst before and after reduction.

ZrO$_2$ support was prepared according to the precipitation method as reported in the literature [39]. The aqueous solution of 0.3 M ZrOCl$_2$ was added to a 0.3 M NH$_4$OH solution at pH of 9–10 under continuous stirring at a drop speed of 1 ml min^{-1}. The hydrous zirconia, after staying in its mother solution for 24 h, was filtered, washed with deionized water until no Cl$^-$ could be detected by using the AgNO$_3$. Then it was washed with ethanol and dried overnight at 110 °C and finally calcined at 700 °C for 5 h.

The loading of LaNi$_{1-x}$Co$_x$O$_3$ on the ZrO$_2$ support was performed according to the citrate complexing method. The support of ZrO$_2$ was impregnated with the aqueous solution of lanthanum, cobalt and nickel nitrate at a La:Ni:Co molar ratio of 1:(1−x):x, in which citric acid in 120% mol of the total cations and polyethylene glycol 400 in 20% molar amount of the citric acid were added. After staying overnight at 80 °C, the resulting sample was dried at 120 °C for 24 h and subsequently calcined at 300 °C and 700 °C for 2 h and 5 h, respectively, with a heating rate of 2 °C min^{-1}. Then the loading process above was repeated, in order to obtain a higher LaNi$_{1-x}$Co$_x$O$_3$ loading amount. The amount of LaNi$_{1-x}$Co$_x$O$_3$ in the calcined support is 32 wt.%. Three samples at a Ni:Co molar ratio of (1−x):x (x = 0, 0.3, 1) were prepared. The so prepared samples were referred to as L-N-Z, L-N-C-Z and L-C-Z for LaNiO$_3$/ZrO$_2$, LaNi$_{0.7}$Co$_{0.3}$O$_3$/ZrO$_2$ and LaCoO$_3$/ZrO$_2$, respectively.

The influence of the Ni/Co ratio on the catalytic performance in the SRE was investigated, and when the mole ratio of Ni:Co was 7:3, the catalyst exhibited the best performance. Therefore, LaNi$_{0.7}$Co$_{0.3}$O$_3$/ZrO$_2$ and LaNi$_{0.7}$Co$_{0.3}$O$_3$ were studied in detail to present the catalyst design scheme. Chen et al. [40] investigated the effect of Ni/Co ratio on the catalytic performance for SRE, and found the similar result, that is, as the mole ratio Ni/Co is 2/1, the catalyst showed the best performance.

2.2. Catalytic performance tests

Catalytic performance tests were carried out on a fixed-bed quartz reactor at atmospheric pressure. 75 mg of catalyst were diluted with SiO$_2$ particles (both 40–60 mesh) in the mass ratio of 1:8 and they were loaded into the reactor. Prior to each reaction, the system was out-gassed with N$_2$ for 10 min, and then reduced in 5 vol.% H$_2$-Ar at 650 °C for 120 min with a flow rate of 50 ml min^{-1}. After reduction the reaction temperature was set at the initial testing temperature. A premixed water-ethanol solution with water to ethanol molar ratio of 3:1 was fed into the reactor through a pump, which was vaporized at 140 °C. The total flow rate of the liquid of water-ethanol was 1.2 ml h^{-1}. The introduced reaction gas mixture was composed of 80 vol% N$_2$ and 20 vol% EtOH + H$_2$O. The resultant gas hourly space velocity (GHSV) of the total gas mixture was 66,000 ml g$_{cat}$$^{-1}$ h^{-1}. For stability tests at GHSV of 264,000 ml g$_{cat}$$^{-1}$ h^{-1}, 25 mg of catalyst was used and the total flow rate of the liquid was increased accordingly.

The effluent gases were analyzed online by using two gas chromatographs with TCD detectors and with two columns of Porapack Q and TDX-01. The Porapack Q packed column was used to analyze water, acetaldehyde, ethanol and acetone. The column temperature was 100 °C and hydrogen was used as the carrier gas. H$_2$, N$_2$, CO, CH$_4$ and CO$_2$ were separated by the TDX-01 column. The column temperature was 80 °C and helium was used as the carrier gas. The reactants from the reactor were heated to gas state before entering into the GC. Nitrogen was used as the internal standard.

The catalytic performance was characterized by two parameters. S$_i$ represents the product distribution of i and ethanol conversion is denoted as X(EtOH). They were calculated according to the following Eqs. of (2.1) and (2.2):

$$X(EtOH) = \frac{n_{in}(Etoh) - n_{out}(Etoh)}{n_{in}(Etoh)} \times 100\% \tag{2.1}$$

$$S_i = \frac{moles(Pi)}{\sum_{i=1}^{n} moles(Pi)} \tag{2.2}$$

where P$_i$ is the molar amount of the product i.

2.3. Catalyst characterization

The BET surface area of the catalysts was determined according to the BET method, and the experimental tests were conducted on a Micromeritics ASAP 2010 apparatus at a partial pressure of 0–0.3.

Temperature programmed reduction (TPR) of the catalysts in a 5% H$_2$-Ar gas mixture at a flow rate of 30 ml min^{-1} was carried out on a Thermo-Finnigan instrument. 50 mg of the catalyst with 100–180 mesh grain size was loaded into a quartz tube reactor. The catalyst was heated in the gas mixture from room temperature with a heating rate of 10 °C min^{-1}.

X-ray diffraction (XRD) tests were performed on a Philips X'pert Pro automated powder diffractometer with graphite-monochromated Cu-Kα (λ = 0.15406 nm) radiation in the Bragg-Brentano parafocusing geometry. The spectra were collected between 2θ ranges of 20°–90°, at a scanning speed of 5° min^{-1}.

Transmission electron microscopy (TEM) measurements were performed on a FEI (PHILIPS) Tecnai-G2F20 instrument equipped with Field Electronic Emitter. Samples were deposited on copper grids with a holey-carbon-film support after ultrasonic dispersion of the catalyst in water-free ethanol.

Thermal analysis of thermogravimetry (TG) was performed on a DTG-50/50H from Shimadzu Corporation from room temperature to 900 °C with a heating rate of 10 °C min^{-1} and in flowing air. 5.0–10.0 mg of catalyst was used. The total weight loss is determined by Eqs. (2.3)

$$\frac{W_1 - W_2}{W_1} \times 100\% \tag{2.3}$$

where W$_1$ is the weight of the reacted catalyst before TG test, and W$_2$ is the weight of the reacted catalyst after the TG test.

3. Results

3.1. Physical properties of the catalysts

The BET surface area of the prepared ZrO$_2$ was 92 m^2 g^{-1}. After loading the perovskite-type oxide, the specific surface area of the resulting LaNi$_{1-x}$Co$_x$O$_3$/ZrO$_2$ was in the 63–67 m^2 g^{-1} range (Table 1). The decrease in the surface area after the loading was most likely due to blockage of the micro- and mesopores by the perovskite-type oxide. However, all of the loaded samples maintained a much higher BET surface area than that of bulk L-N-C, which is beneficial for high dispersion of the active metal components.

The sizes of the metal particles in the reduced and used catalysts are listed in Table 1, and these values were calculated from the XRD results. The metal particles remained small after the stability test. For the used catalysts, all of the metal particles were approximately 11 nm, which was close to that of the reduced catalysts. Therefore, sintering of the catalysts was not serious after the 50 h stability test, and the active Ni-Co nanoparticles exhibited a very good anti-sintering ability.

3.2. TPR results

Fig. 2 shows the TPR profiles of the fresh catalysts and the hydrogen consumption (calculated on the basis of 50 mg catalyst) derived from the experimental results and calculated theoretically, which

Table 1
BET surface areas, amount of metal loaded and weight losses for the used catalysts.

Sample	S_{BET} ($m^2 g^{-1}$)	Metal load (wt%)	D_{metal} (nm)[a]-reduced	D_{metal} (nm)[a]-used for 50 h	TG(%)–50 h
ZrO_2	92	/		/	/
L-N-Z	67	5.4	9	11	50
L-N-C-Z	63	5.4	9	10	32
L-C-Z	64	5.4	10	12	60
L-N-C	19	/	/	/	/

D_{metal} (nm)[a]-reduced: the metal particle size of the reduced catalysts. D_{metal} (nm)[a]-used for 50 h: the metal particle size of the catalysts after stability test.

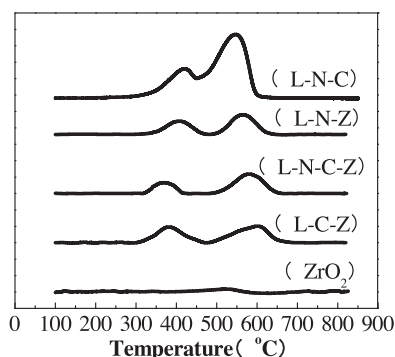[a] Calculated from XRD results using the Scherrer formula: $D = k\lambda/(\beta\cos\theta)$.

Fig. 2. TPR profiles of $LaNi_{1-x}Co_xO_3/ZrO_2$, $LaNi_{0.7}Co_{0.3}O_3$ and ZrO_2.

are listed in Table 2. The hydrogen consumptions were derived by using pure CuO as the basis sample for comparison. A weak peak at approximately 520 °C was observed for the support ZrO_2, which corresponds to a small hydrogen consumption. Therefore, ZrO_2 was barely reduced. A similar reduction trend was observed for the other samples. The H_2-TPR curves for $LaNi_{1-x}Co_xO_3/ZrO_2$ and $LaNi_{0.7}Co_{0.3}O_3$ contained two main peaks. The reduction of Ni^{3+} or Co^{3+} in the perovskite lattice to Ni^{2+} or Co^{2+}, respectively, is responsible for the low temperature peaks observed at 320 °C to 450 °C, and the high temperature peaks corresponded to the reduction of Co^{2+} to Co° and Ni^{2+} to Ni° [41]. The TPR profiles of $LaNi_{1-x}Co_xO_3/ZrO_2$ and $LaNi_{0.7}Co_{0.3}O_3$ are similar, suggesting that the perovskite structure of $LaNi_{1-x}Co_xO_3$ was loaded on the ZrO_2 support.

For all of the catalysts, the experimental hydrogen consumptions are much close to that of the theoretical values for Ni^{3+} to Ni^{2+} and Co^{3+} to Co^{2+} (the low temperature peak) as well as Ni^{2+} to Ni° and Co^{2+} to Co° (the high temperature peak) (Table 2), supporting the assignment of the reduction peaks.

By comparing L-N-C-Z with unsupported $LaNi_{0.7}Co_{0.3}O_3$, the low-temperature reduction peak for L- N-C-Z that was observe at approximately 380 °C shifted to a lower temperature due to the $LaNi_{0.7}Co_{0.3}O_3$ particles that were supported on ZrO_2 being smaller in size. Therefore, these particles possess a higher specific surface energy, resulting in more facile reduction. This result agrees with the viewpoint in [42,43]. In comparison to bulk L-N-C, the high-temperature reduction peak for L- N-C-Z was shifted toward a higher temperature, which may be due to the strong interaction between the metal ions in the perovskite and the support. This

result is in agreement with the viewpoint in [44]. The variation in the reduction temperature as a function of the particle size of the loaded oxide exhibits two trends. For the reduction of Ni^{3+} or Co^{3+} to Ni^{2+} or Co^{2+}, respectively, in the perovskite lattice, the effect of the specific surface energy is the most important. However, for the reduction of Co^{2+} or Ni^{2+} to Co° or Ni°, respectively, the interaction between the oxide and the support is the most important.

For the L- N-C-Z catalyst, Ni^{2+} and Co^{2+} are reduced to Ni° and Co°, respectively, in the same peak in a temperature range from 500 °C to 650 °C. Therefore, the Ni and Co metals formed in one reduction peak, which is beneficial for the formation of the Ni-Co alloy, as expected in the preparation Scheme. The TPR results indicated that the metal ions (i.e., nickel and cobalt) can be completely reduced at 650 °C, which was set as the reduction temperature prior to the catalytic performance tests.

3.3. XRD results

Fig. 3 shows the XRD patterns of the calcined and reduced catalysts. In all of the catalysts, ZrO_2 was in the monoclinic phase. $LaNi_{1-x}Co_xO_3/ZrO_2$ (x = 0, 0.3, 1) exhibited diffraction peaks corresponding to the perovskite structure [30,32] (Fig. 3A). The diffraction peaks corresponding to NiO and Co_3O_4 were not be detected, suggesting that the perovskite phase of $LaNi_{1-x}Co_xO_3$ was loaded on ZrO_2. In addition, by observing the main diffraction peak of the perovskite phase (Fig. 3B), the peak shifted to a higher 2θ value when cobalt ions were doped into the B sites of the PTO. This phenomenon is due to the ionic radius of Ni^{3+} being bigger than that of Co^{3+} (0.0560 nm and 0.0545 nm, respectively). Therefore, the substitution of Co^{3+} for Ni^{3+} leads to a decrease in the lattice plane distance, and 2θ shifts to a higher value. This result agrees with the diffraction peak shifting to a higher 2θ value when a smaller ion is doped into the lattice [27,38]. In contrast, the shift in the 2θ value indicates that the cobalt and nickel ions were incorporated into the PTO lattice. By comparing L- N-C-Z to L- N-C, the 2θ of the diffraction peak corresponding to the perovskite phase shifted to a higher value for the supported sample. As the size of the crystal becomes smaller, the lattice constant decreases, and the lattice distortion increases. Therefore, the lattice spacing decreases, leading to a shift in the peak to a higher 2θ value [44].

Fig. 3(C) shows the XRD patterns of the reduced catalysts. After reduction, the perovskite structure disappeared, and the diffraction patterns of ZrO_2 only changed slightly compared to the fresh samples, indicating that ZrO_2 is stable in the reduction process. The TPR results suggested that the nickel and cobalt ions were com-

Table 2
Hydrogen consumptions of the fresh catalysts.

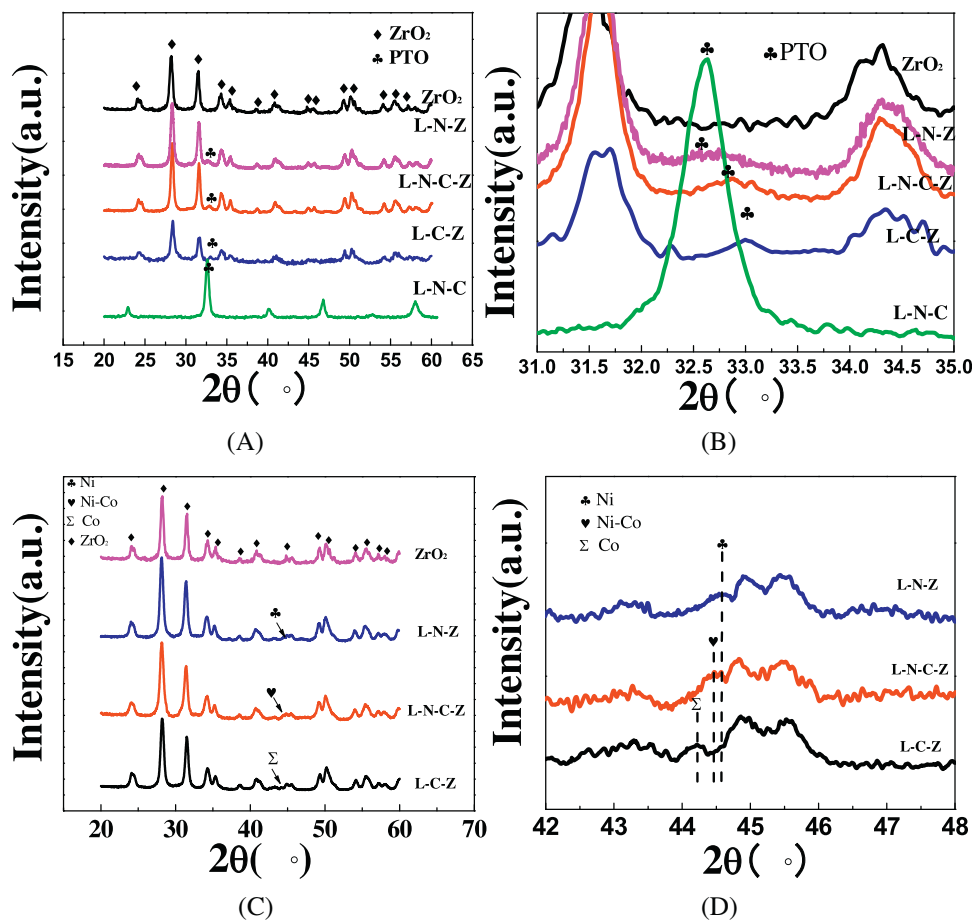| H_2 consumptions(μ mol)	Experiment values		Theoretical values			
	T_L	T_H	$Ni^{3+} \rightarrow Ni^{2+}$	$Co^{3+} \rightarrow Co^{2+}$	$Ni^{2+} \rightarrow Ni^\circ$	$Co^{2+} \rightarrow Co^\circ$
L-N-C	100.2	184.6	71.2	30.5	142.5	61.1
L-N-Z	28.6	52.1	24.7	–	49.4	/
L-N-C-Z	26.3	55.3	17.3	7.4	34.5	14.8
L-C-Z-	32.0	56.5	/	24.7	/	49.4

Fig. 3. XRD patterns of the calcined catalysts (A) along with the magnified patterns for 2θ from 31° to 35°(B) and the reduced catalysts (C) along with the magnified patterns for 2θ from 42° to 48° (D).

pletely reduced to their metallic state after reduction at 650 °C for 2 h. For the reduced samples, the diffraction peaks corresponding to Ni, Co and Ni-Co were observed. The atomic ratio of La/(Ni + Co) in $LaNi_{1-x}Co_xO_3$ was 1. Therefore, the reduction of the nickel and cobalt ions in $LaNi_{1-x}Co_xO_3$ was concomitant with the formation of La_2O_3. However, the diffraction peaks for La_2O_3 were not observed, which may be due to its highly dispersed state. A similar result was reported by Sun, who found that when the loading amount of La_2O_3 on ZrO_2 was higher than 14 wt%, the XRD peak corresponding to La_2O_3 was observed in the XRD patterns [45].

As shown in Fig. 3(D) and Table 3, the metallic peak corresponding Ni-Co in the reduced catalysts was located between the diffraction peaks corresponding to metallic Ni (1 1 1) and Co (1 1 1), and the 2θ values of the peaks were 44.19°, 44.44° and 44.59° for L-C-Z, L- N-C-Z and L-N-Z, respectively. This result indicates that Ni and Co remain as an alloy after the reaction. The particle sizes of the metals derived from the (1 1 1) crystalline plane are listed in Table 1.

All of the metal particles were approximately 10 nm (Table 1). As Ni^{3+} and Co^{3+} were reduced to $Ni°$ and $Co°$, respectively, in the catalysts, the La_2O_3 side product would uniformly mix with the metal particles and interact with each other due to the even distribution of La^{3+} and nickel and cobalt ions in the precursor of $LaNi_{1-x}Co_xO_3$, which favored the promoting effect of La_2O_3 to take place. La_2O_3 is a promoter for the SRE because it can prevent sintering of the active metal as well as formation of the carbon deposit [46,47].

In summary, the XRD and TPR results indicate that the reduced $LaNi_{0.7}Co_{0.3}O_3/ZrO_2$ catalyst consists of Ni-Co alloy nanoparticles supported on ZrO_2 modified with La_2O_3.

3.4. Catalytic performance

3.4.1. SRE reaction

Chemical processes can be made more efficient by better understanding the various reaction steps [48]. Ethanol steam reforming is a substep continuous reaction. In the first step, ethanol is dehydrated to form ethylene or dehydrogenated to form aldehyde. When ZrO_2 is used as the support in the SRE reaction, ethanol is dehydrated, and ethylene is generated at the acidic sites of zirconia [33,48]. Then, ethylene tends to form coke through additional polymerization-carbon chain growth reactions.

Coke formation is the main reason for catalyst deactivation because it can cover the surface of the catalysts as well as the metal active sites. In this study, when the catalysts were reduced, La^{3+} was separated from the PTO of $LaNi_{1-x}Co_xO_3$, and La_2O_3 was generated, as mentioned in the XRD section. La_2O_3 is a type of rare earth metal oxide that contains alkaline sites, which can neutralize the acidic sites on zirconia. Ethylene was not detected among the products. Therefore, ethanol was not dehydrated to form ethylene due to modification of the acidic sites of zirconia by La_2O_3.
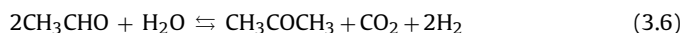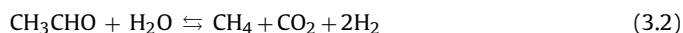
$$CH_3CH_2OH \leftrightarrows CH_3CHO + H_2 \tag{3.1}$$

$$CH_3CHO + H_2O \leftrightarrows CH_4 + CO_2 + 2H_2 \tag{3.2}$$

$$CH_3CHO \leftrightarrows CH_4 + CO \tag{3.3}$$

$$CH_4 + 2H_2O \leftrightarrows CO_2 + 4H_2 \tag{3.4}$$

$$CO + H_2O \leftrightarrows CO_2 + H_2 \tag{3.5}$$

$$2CH_3CHO + H_2O \leftrightarrows CH_3COCH_3 + CO_2 + 2H_2 \tag{3.6}$$

Table 3
2θ value and d-spacing for the diffraction peak at 44.19–44.59° for the reduced catalysts.

Metal particle	Co (1 1 1) for L-C-Z	Ni-Co for L-N-C-Z	Ni (1 1 1) for L-N-Z
interplanar spacing (Å)	2.0478	2.0369	2.0303
2θ in XRD (°)	44.19	44.44	44.59

$$CH_3CH_2OH + 3H_2O(g) \leftrightarrows 6H_2 + 2CO_2 \qquad (3.7)$$
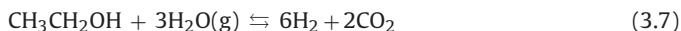
Based on the products shown in Fig. 4, ethanol was dehydrogenated to generate acetaldehyde. Therefore, the SRE reactions on the studied catalysts are as follows: first, ethanol was dehydrogenated to generate acetaldehyde and hydrogen (3.1). Then, at one direction, acetaldehyde was reformed with steam or decomposed to produce methane and CO (CO$_2$) ((3.2) and (3.3)) followed by the methane steam reforming reaction (3.4) and water gas shift reaction (WGSR, 3.5) [49]. At the other direction, acetone was formed (3.6) through a reaction between acetaldehyde and water followed by polymerization of acetone and acetaldehyde that initiates coke formation. Eqs. (3.1) to (3.5) are steps in the SRE that lead to the total SRE shown in Eq. (3.7). The CO/CO$_2$ ratio depends on WGSR, and the hydrogen selectivity is related to the CO/CO$_2$ ratio.

3.4.2. Conversion and selectivity

The catalytic performance of the SRE over the three catalysts was investigated, and the selectivity of the products as well as the ethanol conversion are shown in Fig. 4. For the three catalysts, the loading amount of the active metal was nearly the same (5.4 wt%), and the sizes of the reduced metal particles were similar, as listed in Table 1. The temperature for the complete conversion of ethanol over the L-N-Z, L- N-C-Z and L-C-Z catalysts were 450, 400 and 550 °C, respectively, indicating that the nickel and cobalt metals are quite active for the SRE. The nickel metal was slightly more active than cobalt, and the synergistic effect of the bimetal was obvious because the bimetallic catalyst exhibited the best performance for ethanol conversion.

Based on the selectivity of the products for the L-C-Z catalyst, C$_2$ and C$_3$ products (acetaldehyde and acetone) were generated at low temperatures. The acetaldehyde selectivity over the nickel-containing catalysts was less, and acetone was not detected. In addition, the methane selectivity was higher for the nickel-containing catalyst, which was in accordance with [28,29,50]. Methane is formed by breaking a C—C bond, and more specifically, acetaldehyde was decomposed or reacted with water to produce methane (3.2) and (3.3). Therefore, the C$_2$ products were converted to C$_1$ products in this process. This result supports nickel being more active for breaking C—C bonds than cobalt, as stated in [40,51,52]. It is important to note that the hydrogen selectivity over L-N-Z was lower than that over the L- N-C-Z and L-C-Z catalyst, which may be due to the relatively stronger ability to break C—C bonds on the nickel sites. Therefore, the selectivity to methane was higher, and the selectivity to hydrogen was lower over L-N-Z.

For the L- N-C-Z catalyst, the temperature for the complete conversion of ethanol was the lowest among the three catalysts, and the selectivity to C$_2$ and C$_3$ products was lower than that of the other two catalysts. The selectivity to methane and hydrogen was between that of L-N-Z and that of L-C-Z. In general, L- N-C-Z exhibited the best catalytic performance. Cobalt exhibited high dehydrogenation activity as pointed in [53]; and nickel was good at breaking C—C bonds [51]. Therefore, ethanol was dehydrogenated to generate acetaldehyde on a cobalt site in the Ni-Co alloy, and then, the C—C bond in acetaldehyde was broken on a nickel site in the Ni-Co alloy. This reaction route is much quicker because the C—C bond in acetaldehyde is more easily broken than that in ethanol [27,54]. Therefore, the synergistic effect of cobalt and nickel in the

Ni-Co alloy can substantially improve the catalytic performance for the SRE.

3.4.3. Stability test

To investigate the stability of the catalysts, the catalytic performance was evaluated at a much higher space velocity of 264,000 ml g$_{cat}$$^{-1}$ h^{-1}, and the results are shown in Fig. 5. Based on the results from the stability test for the three catalysts, the sequence of stability was consistent with the order of activity of the catalysts. The bimetallic catalyst exhibited excellent stability in the 50 h test, and the L-N-Z and L-C-Z catalysts began to gradually deactivate during the initial 3 h period. For a short time period (3 h), sintering of the metal can be ignored. Therefore, the deactivation may be due to the formation of coke.

The hydrogen selectivities of the three catalysts were nearly the same during the stability tests but the content of C$_{2+}$ products (acetaldehyde and acetone) varied. This result is in agreement with the conclusion discussed in the conversion and selectivity section.

The synergy of the bimetallic nickel and cobalt maintained the activity of the catalyst for a long period of time. The deactivation of catalysts is typically due to carbon deposition and/or sintering of the metal particles [55–57], and these two aspects will be discussed below.

3.5. Characterization of the catalysts after the stability test

3.5.1. TEM results

The TEM images of the L-N-C-Z catalyst (fresh sample, after reduction and after stability test) are shown in Fig. 6. Based on the representative image of the fresh sample shown in Fig. 6(A), the ZrO$_2$ size is approximately 25 nm, and the ZrO$_2$ is uniformly dispersed. In Fig. 6(B), an approximately 17-nm particle (in the black circle) was observed. Inverse fast Fourier transform (IFFT) analysis was performed on the crystals to determine the phase composition. A lattice distance of 0.273 nm corresponding to perovskite (110) was observed. Lattice distances of 0.228 nm and 0.317 nm due to ZrO$_2$ (0 1 2) and (−1 1 1), respectively, were also observed.

Fig. 6(C) and (D) shows the images of the reduced L-N-C-Z catalyst. Little difference can be seen between the images in Fig. 6(A) and Fig. 6 (C), which indicates that ZrO$_2$ was very stable during the reduction process. In Fig. 6(D), an approximately 6-nm particle (in the yellow circle) was observed, and a lattice distance of 0.2040 nm was observed, which is between that of Co (1 1 1) (0.2046 nm) and Ni (1 1 1) (0.2037 nm). The lattice distance of 0.283 nm was attributed to ZrO$_2$ (1 1 1).

Fig. 6(E) and (F) shows the images of the L-N-C-Z catalyst after the stability test. As shown in Fig. 6(E), the catalyst particles were mostly surrounded by coke. A metal crystal that was approximately 8 nm was supported on ZrO$_2$ and is shown in Fig. 6(F). The size of the metal particle is in agreement with the results calculated from the XRD data (Table 1). A lattice distance of 0.177 nm was observed, and this interplanar crystal spacing was between that of Co (2 0 0) (0.178 nm) and Ni (2 0 0) (0.176 nm), indicating that the Ni-Co alloy is very stable and was not sintered or decomposed after reacting for 50 h.

3.5.2. Line scanning and XRD results

The line scanning profiles for the L-N-C-Z catalyst after the stability test are shown in Fig. 7(A). The line scanning profiles for the
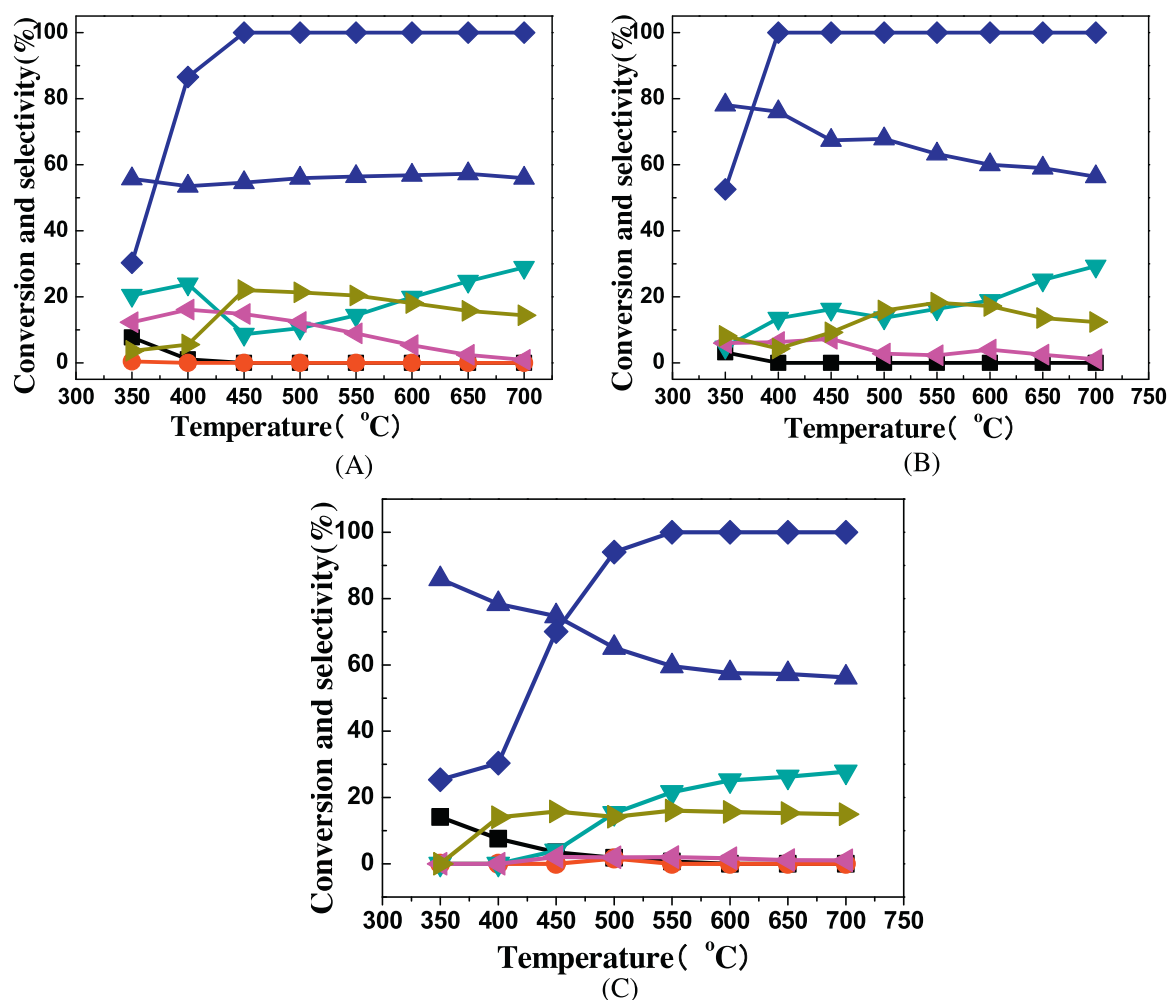
Fig. 4. Variation of the ethanol conversion and selectivity as a function of reaction temperature over (A) L-N-Z, (B) L-N-C-Z and (C) L-C-Z under GHSV = 66, 000 ml g_{cat}^{-1} h^{-1} and steam:ethanol = 3:1 (mole ratio). (CH_3CHO ■, CH_3COCH_3 ●, H_2 ▲, CO ▼, CH_4 ◄, CO_2 ►, Conversion ◆).

Ni and Co elements showed the same variation trend, and the other elements did not exhibit the same variation trend, suggesting the formation and stable existence of the Ni-Co alloy. The size of the metal particles was approximately 8 nm, which is in agreement with the XRD and TEM results.

The enlarged XRD patterns for the L-N-Z, L-N-C-Z and L-C-Z catalysts after the stability tests are shown in Fig. 7 (B). The characteristic diffraction peaks of Co (1 1 1) and Ni (1 1 1) were located at 44.34° and 44.67°, respectively (Table 4). For the used L-N-C-Z catalyst, diffraction peaks corresponding to the monometals were not detected. The diffraction peak for L-N-C-Z was located between the peaks of metallic Ni (1 1 1) and Co (1 1 1) (Fig. 7 (B)). This result indicates that Ni and Co remain as an alloy. In addition, the alloy is very stable during the stability test, which is consistent with the TEM results. The particle sizes of Ni, Ni-Co and Co derived from the (1 1 1) crystalline plane are listed in Table 4. The sizes of the metal particles were all approximately 11 nm after the 50 h stability test, suggesting that the sintering was not serious. This result is consistent with our catalyst design scheme, and the sintering can be prevented by using a support that has a high specific surface area.

3.5.3. Formation of carbon deposit and TG results

$$CH_4 \rightarrow C + 2H_2 \qquad (3.8)$$

$$2CO \rightarrow C + CO_2 \qquad (3.9)$$

Two types of carbon deposits including amorphous carbon, such as coke, and graphitized carbon, such as CNTs, are possible. Both types can be generated during the SRE. Coke is formed from polymerization reactions of C_{2+} products, and graphitized carbon is typically formed via the decomposition of methane and/or the Boudouard reaction, as shown in Eqs. (3.8) and (3.9).

The TG results are shown in Fig. 8, and the data are listed in Table 1. The samples used for the TG analysis are the catalysts obtained after the 50 h stability test. The weight losses were attributed to the combustion of the deposited carbon. In the TG testing process, the metallic nickel and cobalt would be oxidized to oxides, and the weight gain of the oxidation is much smaller compared to the weight loss from carbon combustion. Therefore, the weight gain corresponding to the oxidation was ignored. The amount of carbon deposition decreased from L-C-Z to L-N-Z and L-N-C-Z, indicating that the bimetallic catalyst can reduce the carbon deposition.

According to the literature [58,59], the weight loss from 510 °C to 600 °C was due to the combustion of coke, and the weight loss observed above 700 °C was due to the combustion of graphitized carbon. For the three used catalysts, weight losses above 700 °C were not observed, indicating that the carbon that was formed is primarily coke. This result is consistent with the TEM results.

The absence of graphitized carbon may be due to the following two reasons. First, La_2O_3 can react with CO_2, which
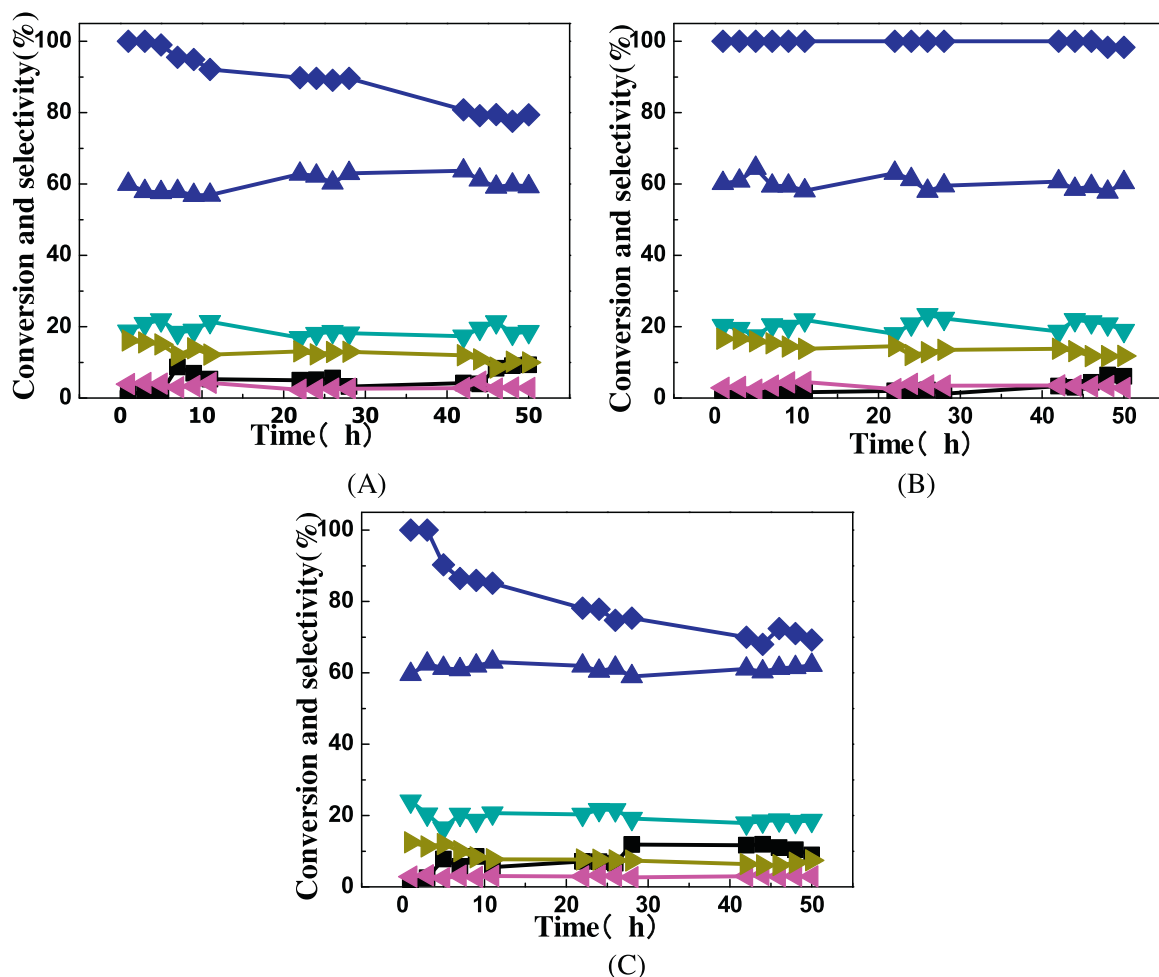
Fig. 5. Variation of the ethanol conversion and selectivity as a function of the reaction time over (A) L-N-Z, (B) L-N-C-Z and (C) L-C-Z for SRE reaction at GHSV = 264, 000 ml g_{cat}^{-1} h^{-1}, steam: ethanol = 3: 1(mole ratio) and 650 °C. (CH$_3$CHO ▇ , H$_2$ ▲ , CO ▼ , CH$_4$ ◀ , CO$_2$ ▶ , Conversion ◆).

Table 4
2θ value and d-spacing for the diffraction peak at 44.32–44.67° for the used catalysts.

Metal particle	Co (1 1 1) for L-C-Z	Ni-Co for L-N-C-Z	Ni (1 1 1) for L-N-Z
interplanar spacing (Å)	2.0412	2.0352	2.0269
2θ in XRD (°)	44.32	44.48	44.67

is a SRE product, to form La$_2$O$_2$CO$_3$, which can eliminate the graphitic carbon deposited through the following reaction: La$_2$O$_2$CO$_3$ + C → La$_2$O$_3$ + 2CO [30]. Second, the addition of ZrO$_2$ can decrease the deposition of graphitic carbon during the methane steam reforming reaction [60]. ZrO$_2$ enhances the dissociation of CO$_2$, which forms oxygen intermediates at the interface between ZrO$_2$ and the active metal, and the oxygen intermediates aid in the elimination of the deposited carbon.

4. Discussion

Coke is a type of amorphous material that typically blocks the active site of metal, which leads to catalyst deactivation. Because sintering of the active metal was not serious, the deactivation of the catalysts was due to the formation of coke, and the good stability of the L-N-C-Z catalyst was due to its good ability to prevent the formation of coke.

The higher anti-coke formation ability of the bimetallic L-N-C-Z catalyst can be explained in two ways. First, coke is formed by the

polymerization of C$_{2+}$ products. The L-N-C-Z catalyst has the lowest selectivity to C$_{2+}$ products. The nano Ni-Co alloy was the best at breaking C—C bonds among the three catalysts, as mentioned in the catalyst performance section. Therefore, the formation of coke is the lowest. Second, coking is a type of surface polymerization reaction between acetaldehyde and acetone. To catalyze this type of reaction, a higher coordination number or larger cluster composed of the same kind active atoms is required. In recent years, it is confirmed in a lot of researches [61,62] that hydrocarbon conversion reaction needs less active atom group than the formation of coking. In the catalyst of L-N-C-Z, nickel and cobalt interact to form Ni-Co alloy and Co atoms can make a dilution effect to Ni atoms, vice versa, cobalt atoms would be diluted by nickel atoms, so the formation of coke by carbon polyethylene reaction is suppressed.

The weight loss for the L-N-C-Z catalyst after the 50 h stability test (mole ratio of water/ethanol = 3 at 650 °C for 50 h with GHSV = 264, 000 ml g_{cat}^{-1} h^{-1}) was 32%. After the 10 h stability test (under the same conditions employed in this study), the weight loss of the best LaFeO$_3$ supported Ni-Co bimetallic catalyst was 49%
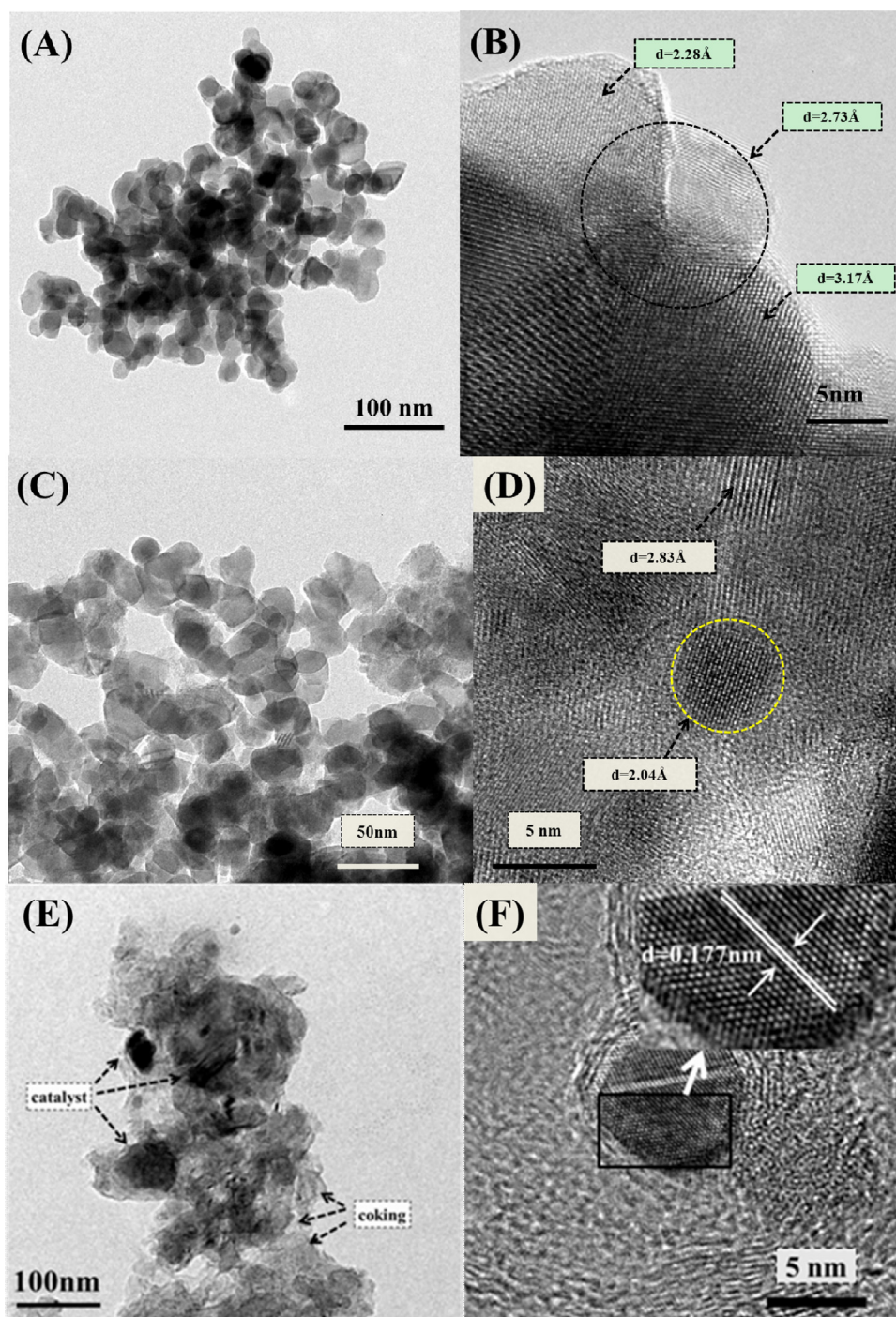
Fig. 6. Representative TEM images of L-N-C-Z (A and B) fresh sample, (C and D) after reduction and (E and F) Used for 50 h.

[30]. After the 30 h stability test (mole ratio of water/ethanol = 3 at 650 °C for 30 h with GHSV = 240,000 ml g_{cat}^{-1} h^{-1}), the weight loss was 45% for the MgO-Al_2O_3 supported Ni-Co bimetallic catalyst [63]. By comparison, the anti-coking ability of L-N-C-Z was relatively good.

The nanoparticles of the active metal really exhibited very good anti-sintering ability, as determined by the XRD and TEM results and the data shown in Table 1. LaNi$_{1-x}$Co$_x$O$_3$/ZrO$_2$ was changed to Ni-Co-La$_2$O$_3$/ZrO$_2$ after the reduction, where La$_2$O$_3$ was highly dispersed on ZrO$_2$ and in contact with ZrO$_2$. The Ni-Co nanoparticles should be deposited on the amorphous La$_2$O$_3$ because both La$_2$O$_3$ and the nanoparticles were confined in the crystal lattice of

LaNi$_{1-x}$Co$_x$O$_3$ prior to reduction. Ni-Co tends to interact with La$_2$O$_3$ because lanthanum, nickel and cobalt can make up a compound of LaNi$_{1-x}$Co$_x$O$_3$. Therefore, the Ni-Co nanoparticles should exhibit very good anti-sintering ability, which is shown in the catalyst design scheme (Fig. 1) in the introduction section. In addition, The Ni-Co alloy nanoparticles appear to possess better anti-sintering ability than the corresponding monometals, which is in agreement with [64] and the data was shown in Table 1. In the reaction process, the structure and composition of the metal nanoparticle surface would be reconstructed to decrease the specific interface energy. The Ni-Co alloy nanoparticles contain two elements, and these nanoparticles are more likely to reconstruct than the nonmetal
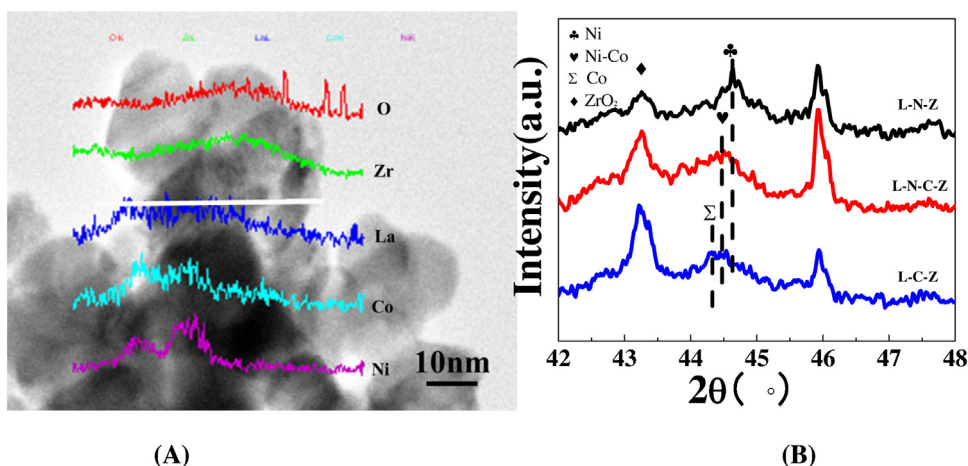
Fig. 7. L-N-C-Z catalysts used for 50 h: (A) line scanning profiles for O, Zr, La, Co and Ni elements and (B) XRD patterns of the magnified pattern for 2θ from 42° to 48°.
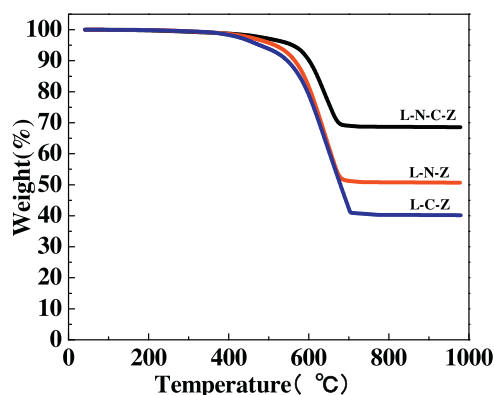

Fig. 8. TG results of the catalysts used for the SRE for 50 h with the same reaction conditions as those listed in Fig. 5.

nanoparticles. Therefore, the Ni-Co alloy nanoparticles are more stable, which may result in better anti-sintering ability. Prasad [65] theoretically studied the effect of the alloy formation on the interface free energy, and the results indicated that the diffusion of the Mg particles was restrained. In addition, the anti-sintering ability improved due to the addition of Zn. This result supports the viewpoint in the previous paragraph to a certain extent.

The hydrogen selectivity over the L-N-C-Z catalyst is in the range of 60% to 65%, which is comparable to that of previously reported catalysts. Chen et al. [66] investigated Co–Ni catalysts derived from hydrotalcite-like materials for the SRE, and the hydrogen selectivity was approximately 65% during the stability test. In another study, Michele and co-workers [33] investigated (Ni, Co, Cu)/(SiO$_2$/ZrO$_2$) catalysts for the SRE, and the hydrogen selectivity was approximately 60%. Molina et al. [67] investigated Ce and Pr-promoted Ni and Co catalysts for the SRE, and the hydrogen selectivity was approximately 65%.

The catalytic activity and stability of the L-N-C-Z catalysts were similar to that of the best Ni-Co bimetallic catalysts in the literature. The Ni-Co/MgO-Al$_2$O$_3$ catalyst was investigated by Yue et al. [63] for SRE, and this catalyst exhibited comparable activity with slightly poorer stability under the same reaction conditions. Resini and co-workers [28] studied yttria-stabilized zirconia (YSZ) supported Ni-Co alloys for SRE (steam/ethanol = 3:1 mol ratio, GHSV = 30, 000 ml g$^{-1}_{cat}$ h^{-1}), and the best catalyst achieved an ethanol conversion of 100% at 400 °C. Guido Busca [68] studied Ni-Co-Zn-Al catalysts for the SRE (steam/ethanol = 3:1 mol ratio, GHSV = 250,000 ml g$^{-1}_{cat}$ h^{-1}), and the ethanol were completely

converted at 500 °C. With respect to stability, the Co-Ni catalysts derived from hydrotalcite-like materials, which were studied by Molina, can maintain 100% ethanol conversion after a 20 h stability test (steam/ethanol = 3/1, GHSV = 22, 000 h^{-1} and 550 °C) [38]. Bilbao et al. [69] investigated Ni-Co catalysts on different supports for SRE, and the catalysts remained active during the 50 h stability test (steam/ethanol = 6/1 and 700 °C).

Our catalytic performance, BET, TPR, XRD, TEM and TG results confirm the catalyst design and preparation scheme mentioned in the introduction section. In the preparation process, LaNi$_{1-x}$Co$_x$O$_3$, which has a perovskite structure, was loaded on the ZrO$_2$ support. After reduction, metal nickel and cobalt are in contact, and a Ni-Co alloy was formed. The characterization of the used catalysts indicated that the deactivation of the catalysts was due to the formation of coke. In addition, the Ni-Co alloy exhibited the best ability to prevent coking.

4.1. Conclusion

A novel preparation method for supported bimetallic alloy nanoparticles was developed in this study. LaNi$_{1-x}$Co$_x$O$_3$, which has a perovskite structure, was loaded on the surface of ZrO$_2$ using the citrate complexation method. The resulting LaNi$_{0.7}$Co$_{0.3}$O$_3$/ZrO$_2$ tends to generate Ni-Co alloy nanoparticles supported on ZrO$_2$ under reduction conditions. In the reduced Ni-Co/ZrO$_2$-La$_2$O$_3$ catalyst, the Ni-Co alloy nanoparticles should be uniformly mixed with La$_2$O$_3$ because they originate from the nano grains of LaNi$_{0.7}$Co$_{0.3}$O$_3$. The LaNi$_{0.7}$Co$_{0.3}$O$_3$/ZrO$_2$ catalyst exhibited good activity and stability for the SRE, indicating that it is an excellent and promising catalyst for the SRE. The good activity was due to the synergistic effect of the Ni-Co alloy nanoparticles on the ZrO$_2$. The good stability was attributed to the decrease in the carbon deposition over the Ni-Co alloy catalyst, which is due to its ability to easily break C—C bonds and to the dilution effect of the Co atoms to/by the Ni atoms. In addition, La$_2$O$_3$ possesses positive promoting effects for eliminating coke. The prepared metal nanoparticles have very good anti-sintering ability due to the interaction between the metal and the lanthanum species as well as the interaction between zirconia and the lanthanum species.

References

[1] N. Bion, D. Duprez, F. Epron, ChemSusChem 5 (2012) 76–84.
[2] J.M. Sun, Y. Wang, ACS Catal. 4 (2014) 1078–1090.
[3] S. Sá, H. Silva, L. Brandao, J.M. Sousa, A. Mendes, Appl. Catal. B 99 (2010) 43–57.
[4] J. Mizeraczyk, K. Urashima, M. Jasinski, M. Dors, Int.J. PEST 8 (2014) 89–97.
[5] J.L. Contreras, J. Salmones, J.A. Colin-Luna, L. Nuno, B. Quintana, I. Cordova, B. Zeifert, C. Tapia, G.A. Fuentes, Int. J. Hydrogen Energy 39 (2014) 18835–18853.
[6] G.A. Deluga, J.R. Salge, L.D. Schmidt, Science 303 (2004) 993–997.
[7] A. Haryanto, S. Fernando, N. Murali, Energy Fuel 19 (2005) 2098–2106.
[8] T. Yamazaki, N. Kikuchi, M. Katoh, T. Hirose, H. Saito, T. Yoshikawa, M. Wada, Appl. Catal. B 99 (2010) 81–88.
[9] M. Bilal, S.D. Jackson, Catal. Sci. Technol. 3 (2013) 754–766.
[10] M. Bilal, S.D. Jackson, Catal. Sci. Technol. 2 (2012) 2043–2051.
[11] I.A. Carbajal Ramos, T. Montini, B. Lorenzut, H. Troiani, F.C. Gennari, M. Graziani, P. Fornasiero, Catal. Today 180 (2012) 96–104.
[12] D. Li, L. Zeng, X.Y. Li, X. Wang, H.Y. Ma, S. Assabumrungrat, J.L. Gong, Appl. Catal. B 176–177 (2015) 532–541.
[13] C.F. Wu, P.T. Williams, Appl. Catal. B 102 (2011) 251–259.
[14] J. Llorca, J.A. Dalmon, P.R. de la Piscina, N. Homs, Appl. Catal. A 243 (2003) 261–269.
[15] S.R. Li, C.X. Zhang, Z.Q. Huang, G.W. Wu, J.L. Gong, Catal. Commun. 49 (2013) 4226–4228.
[16] E. Finocchio, I. Rossetti, G. Ramis, Int. J. Hydrogen Energy 38 (2013) 3213–3225.
[17] A.J. Vizcaíno, A. Carrero, J.A. Calles, Hydrogen Production: Prospects and Processes, first ed., Nova Science Publishers Inc., New York, 2012.
[18] A. Bshish, Z. Yaakob, B. Narayanan, R. Ramakrishnan, A. Ebshish, Chem. Pap. 65 (3) (2011) 251–266.
[19] S.H. Ogo, T. Shimizu, Y. Nakazawa, K. Mukawa, D. Mukai, Y. Sekine, Appl. Catal. A 495 (2015) 30–38.
[20] W.Q. Xu, Z.Y. Liu, A.C. Johnston-Peck, S.D. Senanayake, G. Zhou, D. Stacchiola, E.A. Stach, J.A. Rodriguez, ACS Catal. 3 (2013) 975–984.
[21] V. Palma, F. Castaldo, P. Ciambelli, G. Iaquaniello, Appl. Catal. B 145 (2014) 73–84.
[22] S. Abelló, E. Bolshak, D. Montané, Appl. Catal. A 450 (2013) 261–274.
[23] V.A. Sadykov, S.N. Pavlova, G.M. Alikina, N.N. Sazonova, N.V. Mezentseva, M.V. Arapova, V.A. Rogov, T.A. Krieger, A.V. Ishchenko, R.V. Gulyaev, A.V. Zadesenets, A.C. Roger, C.E. Chan-Thaw, O.L. Smorygo, Chemistry and Catalytic Performance, first ed., Nova Science Publishers Inc., New York, 2013.
[24] H.Q. Chen, H. Yu, F. Peng, H.J. Wang, J. Yang, M.Q. Pan, J. Catal. 269 (2010) 281–290.
[25] K.H. Lin, C.B. Wang, S.H. Chien, Int. J. Hydrogen Energy 38 (2013) 3226–3232.
[26] D. Zanchet, J.B.O. Santos, S. Damyanova, J.M.R. Gallo, J.M.C. Bueno, ACS Catal. 5 (2015) 3841–3863.
[27] S. Andonov, C.N. de Avil, K. Arishtirov, J.M.C. Bueno, S. Damyanova, Appl. Catal. B 105 (2011) 346–360.
[28] C. Resini, M.C.H. Delgado, S. Presto, L.J. Alemany, P. Riani, R. Marazza, G. Ramis, G. Busca, Int. J. Hydrogen Energy 33 (2008) 3728–3735.
[29] N. Homs, J. Llorca, P.R. de la Piscina, Catal. Today 116 (2006) 361–366.
[30] Z.J. Wang, C.X. Wang, S.Q. Chen, Y. Liu, Int. J. Hydrogen Energy 39 (2014) 5644–5652.
[31] F. Liu, Y.H. Qu, Y.Z. Yue, G.L. Liu, Y. Liu, RSC Adv. 5 (2015) 16837–16846.
[32] S.Q. Chen, Y. Liu, Int. J. Hydrogen Energy 34 (2009) 4735–4746.
[33] I. Rossetti, J. Lasso, V. Nichele, M. Signoretto, E. Finocchio, G. Ramis, A.D. Michele, Appl. Catal. B 150–151 (2014) 257–267.
[34] V. Nichele, A. Iwanska, M. Signoretto, F. Menegazzo, I. Rossetti, G. Cruciani, F. Vindigni, G. Cerrato, 11th European Congress on Catalysis - Europa Cat-XI, Lyon, France, September 1st-6th, 2013.
[35] J.A. Villoria, M.C. Alvarez-Galvan, R.M. Navarro, Y. Briceño, F. Gordillo Alvarez, F. Rosa, J.L.G. Fierro, Catal. Today 138 (2008) 135–140.
[36] S. Colonna, S. De Rossi, M. Faticanti, I. Pettiti, P. Porta, J. Mol. Catal. A 187 (2002) 269–276.
[37] S. Cimino, R. Pirone, L. Lisi, Appl. Catal. B 35 (2002) 243–254.
[38] M. Munoz, S. Moreno, R. Molina, Int. J. Hydrogen Energy 39 (2014) 10074–10089.
[39] G. Chuah, S. Jaenicke, B. Pong, J. Catal. 175 (1998) 80–92.
[40] L. Chen, C.K.S. Choong, Z.Y. Zhong, L. Huang, Z. Wang, J.Y. Lin, Int. J. Hydrogen Energy 37 (2012) 16321–16332.
[41] H.Q. Chen, H. Yu, F. Peng, G.X. Yang, H.J. Wang, J. Yang, Y. Tang, Chem. Eng. J. 160 (2010) 333–339.
[42] C.A. Muller, M. Maciejewski, R.A. Koeppel, A. Baiker, J. Catal. 166 (1997) 36–43.
[43] P. Burattin, Mi. Che, C. Louis, J. Phys. Chem. B 103 (1999) 6171–6178.
[44] N. Wang, X.P. Yu, Y. Wang, W. Chu, M. Liu, Catal. Today 212 (2013) 98–107.
[45] H. Sun, Y. Ding, J. Duan, Q. Zhang, Z. Wang, H. Lou, X. Zheng, Bioresour. Technol. 101 (2010) 953–958.
[46] G. Pecchi, P. Reyes, R. Zamora, J. Solid State Chem. 18 (2008) 905–912.
[47] B.P. Barbero, J.A. Gamboa, L.E. Cadus, Appl. Catal. B 65 (2006) 21–30.
[48] R. Padilla, M. Benito, L. Rodriguez, A. Serrano, G. Munoz, L. Daza, Int. J. Hydrogen Energy. 35 (2010) 8921–8928.
[49] G. Nahar, V. Dupont, Biofuels 3 (2012) 167–191.
[50] T.S. Moraes, R.C.R. Neto, M.C. Ribeiro, L.V. Mattos, M. Kourtelesis, S. Ladas, X. Verykios, F.B. Noronha, Appl. Catal. B 181 (2016) 754–768.
[51] M. Ni, D. Leung, M. Leung, Int. J. Hydrogen Energy 32 (2007) 3238–3247.
[52] P. Bichon, G. Haugom, H.J. Venvik, A. Holmen, E.A. Blekkan, Top. Catal. 49 (2008) 38–45.
[53] M.S. Batista, R.K.S. Santos, E.M. Assaf, J.M. Assaf, E.A. Ticianelli, J. Power Sources 134 (2004) 27–32.
[54] S. Velu, K. Suzuki, M. Vijayaraj, S. Barman, C.S. Gopinath, Appl. Catal. B. 55 (2005) 287–299.
[55] S. Freni, S. Cavallaro, N. Mondello, L. Spadaro, F. Frusteri, J. Power Sources 108 (2002) 53–57.
[56] F. Frusteri, S. Freni, V. Chiodo, J. Power Sources 132 (2004) 139–144.
[57] F. Frusteri, S. Freni, V. Chiodo, Appl. Catal. A 270 (2004) 1–7.
[58] S. Natesakhawat, R.B. Watson, X. Wang, J. Catal. 234 (2005) 496–508.
[59] M.C. Sanchez-Sanchez, R.M. Navarro, J. Fierro, Int. J. Hydrogen Energy 32 (2007) 1462–1471.
[60] S. Therdthianwong, C. Siangchin, A. Therdthianwong, Fuel Process. Technol. 89 (2008) 160–168.
[61] J.R. Rostrup-Nielsen, Catal. Sci. Technol. 5 (1984) 1–5.
[62] N. Rahemi, M. Haghighi, A.A. Babaluo, M.F. Jafarid, S. Khorram, Int. J. Hydrogen Energy 38 (2013) 16048–16061.
[63] Y.Z. Yue, F. Liu, L. Zhao, L.H. Zhang, Y. Liu, Int. J. Hydrogen Energy 40 (2015) 7052–7063.
[64] G.P. Szijarto, A. Tompos, J.L. Margitfavi, Appl. Catal. A 391 (2011) 417–426.
[65] O. Sivakesavam, Y.V.R.K. Prasad, Mater. Sci. Eng. A 362 (2003) 118–124.
[66] L. He, H. Berntsen, E. Ochoa-Fernandez, J.C. Walrnsley, E.A. Blekkan, D. Chen, Top. Catal. 52 (2009) 206–217.
[67] M. Munoz, S. Moreno, R. Molina, Int. J. Hydrogen Energy 37 (2012) 18827–18842.
[68] G. Busca, U. Costantino, T. Montanari, G. Ramis, C. Resini, M. Sisani, Int. J. Hydrogen Energy 35 (2010) 5356–5366.
[69] A.G. Gayubo, J. Vicente, J. Erena, C. Montero, M. Olazar, J. Bilbao, Catal. Lett. 144 (2014) 1134–1143.